Understanding Oligonucleotide-Templated Nanocrystals: Growth Mechanisms and Surface Properties

Tae-Gon Cha,[†] Benjamin A. Baker,[†] Janette Salgado,[†] Christopher J. Bates,[†] Kok Hao Chen,[§] Alice C. Chang,[§] M. Cem Akatay,[‡] Jae-Hee Han,[⊥] Michael S. Strano,[§] and Jong Hyun Choi[†,*]

[†]School of Mechanical Engineering, Birck Nanotechnology Center, Bindley Bioscience Center, Purdue University, West Lafayette, Indiana 47907, United States, [‡]School of Materials Engineering, Birck Nanotechnology Center, Purdue University, West Lafayette, Indiana 47907, United States, [§]Department of Chemical Engineering, Massachusetts Institute of Technology, Cambridge, Massachusetts 02139, United States, and [⊥]Department of Energy & Information Technology, Gachon University, Seongnam-si, Gyeonggi-do, 461-701, South Korea

ABSTRACT We describe studies of nanoparticle synthesis using oligonucleotides as capping ligands. The oligonucleotides nucleate, grow, and stabilize near-infrared fluorescent, approximately uniform PbS nanocrystals in an aqueous environment. The properties of the resulting particles strongly depend upon the sequences as well as synthesis conditions. Fourier Transform infrared measurements suggest that functional groups on the nucleobases such as carbonyl and amine moieties are responsible for surface passivation, while the phosphate backbone is strained to accommodate nucleobase bonding, preventing irreversible aggregation and thereby stabilizing the colloids. Our theoretical model indicates that oligonucleotide-mediated particle growth relies on the chemical reactivity of the oligonucleotide ligands that saturate dangling bonds of growing clusters, and favorable sequences are those that have the highest surface reactivity with growing particles. The oligonucleotide template approach is facile and versatile, offering a route to produce a range of material compositions for other chalcogenide semiconductor quantum dots and metal oxide nanoparticles.

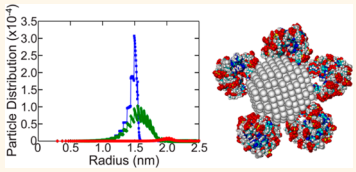

KEYWORDS: template synthesis · oligonucleotides · nanocrystals · capping chemistry · particle growth

Biofunctionalized colloidal nanocrystals have received much attention in the past decade because of their potential and promise in biomedical detection and therapeutics.[1−3] Particularly, semiconductor quantum dots and magnetic nanoparticles have been examined as contrast agents for *in vivo* fluorescence and magnetic resonance imaging.[4−6] For such applications, uniform nanocrystals with well-defined shapes and properties are desired and often synthesized *via* wet chemistry using small organic ligands. Subsequent ligand exchange or additional encapsulation of nanocrystals with polymer, silica, or phospholipids is required during the preparation to render them water-soluble and to enable further conjugation chemistry for molecular recognition and targeting.[7,8] This additional step may introduce unwanted sample heterogeneity, surface defects on the nanocrystals, and an overall increase in the size of nanoparticle construct.[3]

An alternative approach to nanocrystal fabrication and functionalization is to nucleate and cap nanocrystals by directly using functional biomolecular ligands such as nucleic acids.[9−11] We previously discovered that a class of DNA aptamers—oligonucleotides that are typically identified *via* evolutionary *in vitro* selection processes and bind specifically to a molecular target—can stabilize colloidal nanocrystals in aqueous solution and retain the inherent target recognition ability.[12,13] Thus, the oligonucleotides serve two purposes of particle growth control and target recognition. This synthesis includes a single-step procedure performed at room temperature and is fundamentally different from thiol-modified DNA grafting to premade particles in that part of the oligonucleotides actually passivate the dangling bonds of the growing nanoclusters in the reaction chamber, stabilizing the colloids in aqueous solution. Compared to conventional organic-based synthesis, this facile approach is less laborious and utilizes only biomolecular ligands for surface capping, often resulting in less cytotoxicity.[14]

The simplicity of this synthesis method belies the underlying mechanistic complexity. Although the particle growth and stabilization processes have been actively studied,[15,16] the actual molecular capping mechanisms at the biomolecular−inorganic interface still are not well understood. In a recent study, the primary amine and phosphate group of the mononucleotides

* Address correspondence to jchoi@purdue.edu.

Received for review June 22, 2012 and accepted August 29, 2012.

Published online August 29, 2012
10.1021/nn302779m

were identified to be the functional groups responsible for nucleation, nanoparticle growth, and colloid stabilization.[17] However, this study does not reveal the full nature of the nanoparticle makeup. In further studies, structure-specific binding schemes have been proposed for oligonucleotide-mediated particle synthesis, which are strongly associated with the conformation of the nucleic acids.[18,19] The effect of the secondary conformation further complicates the analysis. In this work, we ask whether oligonucleotide-templated nanocrystal synthesis can be generalized to any oligonucleotide sequences by investigating their growth mechanisms experimentally and theoretically. Using Fourier transform infrared (FTIR) spectroscopy, we find that the chemical binding affinity of the nucleobases and steric effect of the DNA's backbone structure play important roles in forming stable nanocrystals. From these data sets, we propose a theoretical model, based upon LaMer's burst nucleation model,[20] to describe oligonucleotide-templated nanocrystal synthesis processes with the reactivity of nucleobases to the nanocrystal surface as a major parameter. We have used chalcogenide nanocrystal quantum dots (*e.g.*, lead sulfide or PbS) as a model system, which fluoresce in the near-IR, and also explored if the same capping chemistry can be used for other types of nanocrystals such as iron oxides.

RESULTS AND DISCUSSION

Oligonucleotide-Capped Nanocrystals. Ten different, single-stranded, short-chain DNA sequences are examined for their ability to cap and stabilize growing nanocrystals in aqueous solution at room temperature. The nanocrystal solutions were washed several times to remove unbound excess DNA and reactant molecules before characterization (see Methods for detailed procedure). Figure 1a shows the normalized, near-IR photoluminescence (PL) spectra of PbS nanocrystals that are synthesized with five 30-mer DNA strands, a 15 base-long thrombin-binding aptamer (TBA), and a 26 base-long AS1411 as capping ligand at a molar ratio of DNA/S^{2-}/Pb^{2+} = 1:2:4. The 30-mer sequences have repetitive nucleobases; for example, the $d(G_4T)_6$ strand has four successive guanines (G) and a thymine (T), which collectively repeat six times. TBA specifically binds to serine protease thrombin, thereby inhibiting the blood coagulation cascade, and AS1411 has been developed as growth inhibitors for breast cancer cells by targeting nucleolin.[21−23] The DNA-templated nanocrystals exhibit moderately variable emission with the peak wavelengths ranging from 980 to 1080 nm depending on the sequence (Figure 1a). The full widths at half-maximum (fwhm) remain relatively constant at approximately 200 nm (Figure 1b). The PL spectra also indicate that the particle size roughly ranges from 3 to 4 nm,[24] as seen in the transmission electron microscope (TEM) images of TBA-templated PbS nanocrystals (Figure 1c). The TEM images of PbS particles synthesized with $d(GT)_{15}$ at two different molar ratios (DNA/S^{2-}/Pb^{2+} = 1:2:4 and 1:20:40) in Figure 1d and e show that smaller particles with more uniform properties are formed at a lower molar ratio (also see Figure S1 in the Supporting Information). The statistical analysis of the TEM images confirms that the 1:20:40 condition generates relatively larger particles with a broader size distribution (Figure 1f). The Gaussian curve fits indicate that the PbS nanocrystals grown at the 1:2:4 ratio have an average diameter close to 3 nm, while approximately 4 nm diameter particles are produced on average at the higher reactant molar ratio. This trend is anticipated because a relatively smaller amount of DNA (or greater amount of the reactants) allows larger sized nanocrystals to form. Similarly, the PL emission can be tuned by varying the reactant concentrations relative to DNA ligands in the reaction chamber (Figure 1g). When the molar ratio of the reactants (*i.e.*, DNA/S^{2-}/Pb^{2+}) increases from 1:2:4, to 1:20:40, to 1:200:400, significant red-shifts are observed with increasing peak wavelengths, approximately from 978, to 1048, to 1330 nm, respectively. We also note that an increase of the reactant molar ratio above a threshold may result in instability of the colloids due to the lack of capping ligands. The length of the oligonucleotides plays a moderate role in the emission properties of the resulting nanocrystals under our experimental conditions, as shown in Figure 1h, where 10, 20, and 30 base-long poly GT strands have been used to synthesize nanocrystals. Longer wavelength emission is observed with shorter sequences, likely because longer strands offer more binding sites to saturate the surface of the growing clusters at the given concentration, forming relatively smaller nanocrystals. While the various DNA oligonucleotides explored here result in forming bright semiconductor nanocrystals, the relative emission efficiency is strongly dependent upon the sequences (Figure 1i).

We observed that the same capping chemistry can be applied for other chalcogenide nanocrystals such as CdS that fluoresce in the visible with emission characteristics dependent upon DNA ligands (Figure S2), which other groups also reported in recent years.[25−27] In this study, we find that oligonucleotide ligands are also useful in growing and stabilizing other types of nanocrystals such as Fe_3O_4 magnetic particles with some notable differences. For Fe_3O_4 nanocrystals, the one-pot synthesis at room temperature may be employed similar to chalcogenide nanocrystals, but particle formation is initiated by a change in pH of an aqueous mixture solution of ferric and ferrous precursor molecules (Fe^{2+}/Fe^{3+} = 1:2) in the presence of DNA ligand template.[28,29] The size of the iron oxide nanocrystals resulting from the reductive precipitation was examined by TEM and dynamic light scattering, which

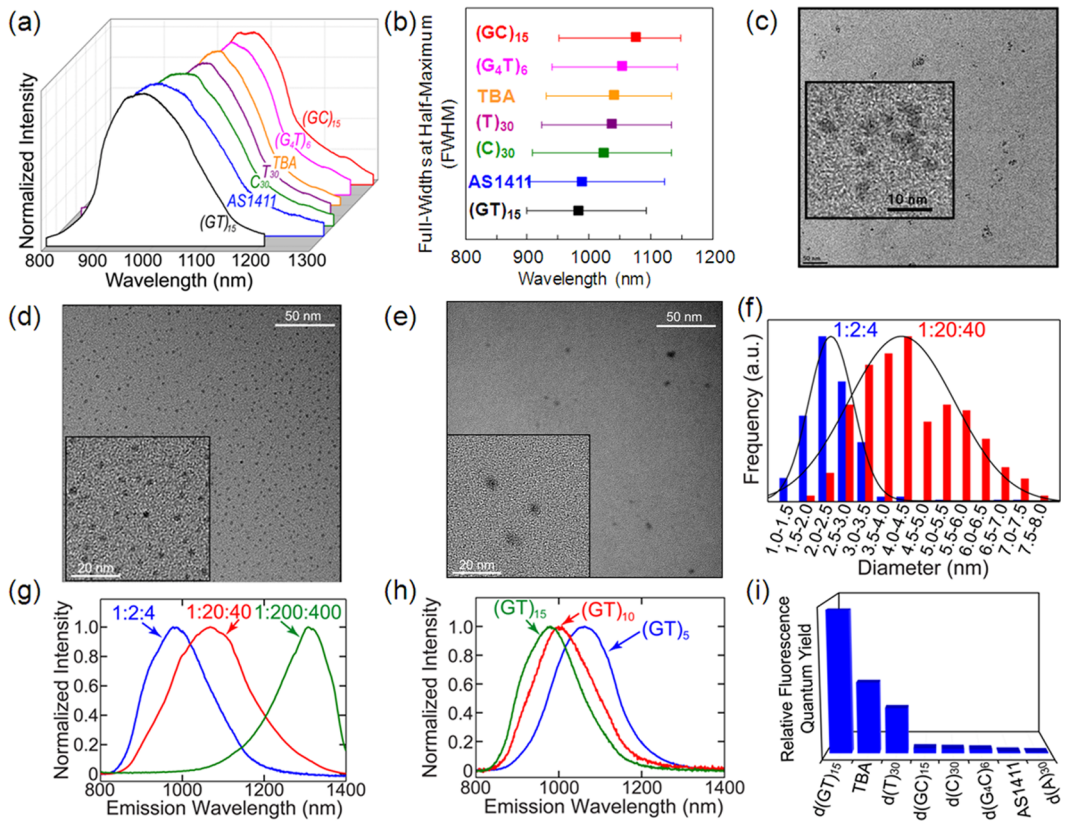

Figure 1. PbS nanocrystals synthesized in aqueous solution with various DNA ligand templates. (a) Normalized near-IR PL spectra of the nanocrystals synthesized using 7 different DNA sequences at a molar ratio of DNA/S^{2-}/Pb^{2+} = 1:2:4. These strands include 30 repetitive nucleobases, 15 base-long TBA, and 26-mer AS1411. (b) Emission peak wavelengths and fwhm extracted from the fluorescence spectra in (a). (c) TEM images of PbS nanocrystals synthesized using TBA. The scale bar indicates 50 nm, while the scale in the inset is 10 nm. TEM images of PbS nanocrystals grown with 30-mer poly GT DNA alternating guanine and thymine at molar ratios of DNA/S^{2-}/Pb^{2+} = 1:2:4 (d) and 1:20:40 (e). (f) Statistical analysis of PbS particle size distributions from (d) and (e) with Gaussian curve fits. (g) PL spectra of PbS nanocrystals synthesized with $d(GT)_{15}$ ligands at three different molar ratios of reactants (*i.e.*, DNA/S^{2-}/Pb^{2+}). (h) PL spectra of nanocrystals synthesized with poly GT as a function of the sequence lengths. (i) Relative PL quantum yields of PbS nanocrystals as a function of DNA sequence.

measure electron-dense core size and hydrodynamic diameter of colloidal particles, respectively (Figure 2). Figure 2a presents that Fe_3O_4 nanocrystals have a hydrodynamic diameter of roughly 80 nm at the ratio of DNA/Fe^{2+}/Fe^{3+} = 1:2:4, and the diameter decreases with increasing precursor concentrations at a fixed DNA amount. This trend of increasing particle size with higher ligand concentration is opposite to what is observed with the PbS nanocrystals, but is expected in the noninjection one-pot synthesis of iron oxide nanoparticles due to a higher supersaturation ratio.[30,31] The Fe_3O_4 nanocrystals appear to have broader size distributions compared to chalcogenide nanocrystals. Previous studies also showed that the pH change-induced iron oxide particles have bimodal size distributions where superparamagnetic and ferrimagnetic magnetites coexist.[28] In spite of these differences, we show below that the chemical nature of the oligonucleotide stabilization in this case is almost identical to the PbS system.

Coordination Chemistry. The strong influence of DNA sequences on the emission efficiency suggests that DNA bases and their arrangement are predominant parameters in the capping chemistry. We used FTIR spectroscopy to provide insight into the chemical nature of the capping. Figure 3a–c present the vibrational spectra of DNA bases, where critical differences are observed between free and coordinated DNA, while the spectra of DNA-templated PbS and Fe_3O_4 nanocrystals are almost identical (Figure 3a and d). The 1687 cm^{-1} peak, corresponding to the C6═O6 stretching, N1–H bending, or $-NH_2$ scissoring of guanine,[32] is shifted to 1694 cm^{-1} for $d(GT)_{15}$, is broadened for TBA, and remains relatively unchanged for $d(G_4T)_6$ on the nanocrystals. We assign the perturbation of this peak to the potential coordination bonding of these functional groups to the metal cations on the particle surface. Interestingly, the degree of the perturbation appears to be associated with the quality of the nanocrystals, as the $d(G_4T)_6$-templated nanocrystals with minimal perturbation in the FTIR spectra exhibit dim emission (*i.e.*, relatively low PL quantum efficiency) compared to those synthesized with the other two sequences. On the particle surface, the dG:C8═N7 peak at ~1533 cm^{-1} of poly GT is enhanced (shown as a solid star in Figure 3a), while the dG:C2═N3 peak

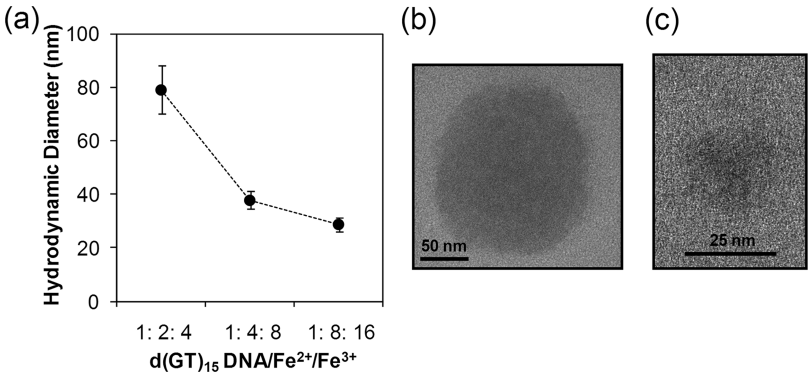

Figure 2. Fe_3O_4 nanocrystals synthesized with 30 base-long poly GT as capping ligand. (a) Hydrodynamic diameters of the iron oxide nanocrystals synthesized at various molar ratios of iron precursor and DNA ligand. An increase of the precursor concentration relative to DNA leads to smaller nanoparticles. TEM images of Fe_3O_4 nanocrystals at DNA/Fe^{2+}/Fe^{3+} of 1:2:4 (b) and 1:4:8 (c).

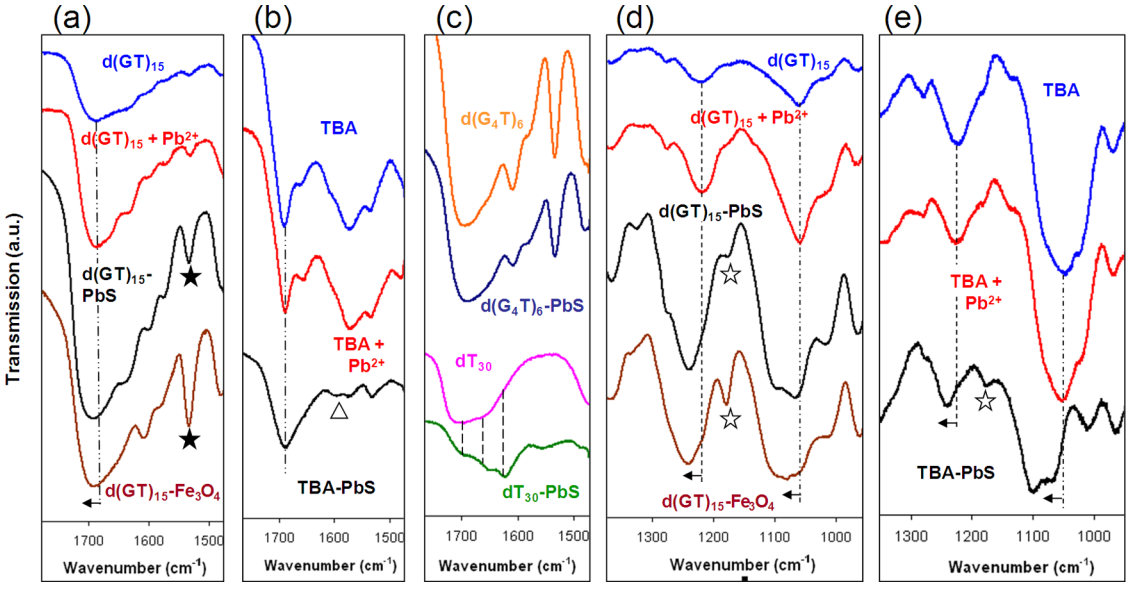

Figure 3. FTIR spectra of DNA strands that are free and bound to nanocrystals. Vibrational signatures of nucleobases are shown in (a) through (c), while those of the DNA phosphate backbone are presented in (d) and (e). (a and d) Free $d(GT)_{15}$, $d(GT)_{15}$ with Pb^{2+}, $d(GT)_{15}$-templated PbS, and Fe_3O_4 nanocrystals. (b and e) Free thrombin-binding aptamer or TBA, TBA with Pb^{2+}, and TBA-templated PbS nanocrystals. (c) Free $d(G_4T)_6$ and $d(T)_{30}$, and the same sequences on the nanocrystals. The particles were washed to remove excess DNA and ions before deposition on IR sample cards for characterization. The spectra are offset for clarity. The FTIR spectra of DNA-templated PbS and Fe_3O_4 nanocrystals are almost identical, indicating that this capping chemistry may be extended to a spectrum of materials.

at ~1573 cm^{-1} of TBA diminishes notably,[33] illustrating the roles of N3 and N7 on binding (shown as an open triangle in Figure 3b). The free T and T-QD spectra in Figure 3c show that the peak intensities of C2═O2 stretching (1696 cm^{-1}) and the ring (1623 cm^{-1}) reverse when the DNA is bound to particles, and the C4═O4 stretching (1663 cm^{-1}) peak is shifted to 1653 cm^{-1}.[33,34] The perturbation of the ring vibration may be viewed as tilting of the base to accommodate binding of two thymine carbonyls to nanocrystals. The FTIR results of the nucleobases suggest that the carbonyl groups play critical roles in surface passivation, while amines and other nitrogen moieties contribute. This hypothesis is also supported by our observation that nanocrystals capped by poly A, which does not have a carbonyl group, exhibit very dim emission properties compared to those formed with other sequences including poly GT, TBA, poly T, and poly C (Figures 1i and S3). In contrast, 15 base-long poly U that contain two carbonyl groups indeed resulted in stable, bright nanocrystals (Figure S4).

In addition to the possible roles of oxygen groups in the DNA phosphate backbone in particle growth and capping,[10] we hypothesize that the nucleobase interactions with nanocrystals may result in a twist of the DNA backbone, extending from the particle surface and serving as negatively charged ligands that stabilize the colloids. The vibrational signatures of the backbone are examined as shown in Figure 3d and e. The antisymmetric PO_2^- stretching of poly GT and

TBA is shifted from approximately 1220 to 1240 cm^{-1} ($\Delta\eta$ = ~20 cm^{-1}) when bound to particles.[35] The symmetric PO_2^- stretching at ~1080 cm^{-1} of free $d(GT)_{15}$ and TBA overlaps with furanose CO stretching at 1050 cm^{-1}.[35] However, the PO_2^- stretching of the DNA bound on particles becomes prominent and shifted to nearly 1100 cm^{-1}, while the CO stretching peak is shifted to 1065 cm^{-1}, which we attribute to steric or torsional strain in the backbone. Since a number of DNA molecules passivate each nanocrystal, the strands not only bind to the particle but also interact with each other, which may induce a steric effect or secondary conformation change. These effects are analogous to the case of peptides attached to Au nanoparticles[36] and to the G-rich oligonucleotide DNA aptamers that form a G-quadruplex structure.[34] If the bound DNA adopts either a G-quadruplex or a compact A-form-like structure, its backbone may be twisted to optimize the spatial arrangement for base binding to the particle surface. The C3′-endo-type sugar peak at 1178 cm^{-1}, a marker of A-form DNA indicated as open stars in Figure 3d and e, is notably enhanced in the bound DNA spectra.[35] The ~20 cm^{-1} shift of the symmetric PO_2^- stretching is likely associated with a G-quadruplex formation, maximizing guanine stacking.[34] The secondary structure formation is also supported by our previous observation of the G-quadruplex formation of TBA and AS1411 strands while capping the nanocrystal surface.[12,13] Overall, our mechanisms suggest that the carbonyl groups and amine/nitrogen moieties of nucleobases primarily coordinate to cations on the particle surface, enabled by the phosphate backbone twist and/or secondary structure formation, and the overhanging backbone prevents irreversible aggregation of the particles.

Prediction of Nucleic Acid-Mediated Nanocrystal Growth. We hypothesize that oligonucleotide-mediated particle growth relies on the chemical reactivity of the oligonucleotide ligands that saturate dangling bonds of growing clusters, thereby stabilizing the colloids. Favorable sequences are those that have the highest surface reactivity with growing particles. To illustrate how this leads to the formation of stable nanocrystals with uniform properties, we performed numerical simulations of DNA-mediated PbS nanocrystal growth and examined the capability of surface reactivity of oligonucleotide strands to recognize and bind a growing nanocrystal. In our model that adopts LaMer's burst nucleation theory,[20] precursor ions add sequentially to the growing cluster (*AB*) such that approximate electroneutrality is maintained (*i.e.*, there is no unbounded gain in charge). Hence, the concentrations of precursors, A (= Pb^{2+}) and B (= S^{2-}), are equal at all times. The parameter C_i is a stable, DNA-capped particle of Pb^{2+}-S^{2-} pairs numbering i total, while $(AB)_i$ represents a metastable, growing cluster of i ion pairs.

$$A + B \underset{k_1/K_1}{\overset{k_1}{\rightleftarrows}} (AB)_1 \quad (1)$$

$$A + B + (AB)_i \underset{k_{i+1}/K_{i+1}}{\overset{k_{i+1}}{\rightleftarrows}} (AB)_{i+1} \quad (2)$$

$$(AB)_i + n(i)Q \underset{k_q/K_q}{\overset{k_q}{\rightleftarrows}} C_i \quad (3)$$

The three reactions are (1) nucleation, (2) cluster growth, and (3) cluster capping. Here, Q denotes the DNA concentration. Parameters k_i and K_i are the forward reaction rate and equilibrium constants of the A and B reaction, respectively. The value of K_i can be estimated from nucleation thermodynamics.[20] Similarly, k_q and K_q are the rate and equilibrium constants of the DNA capping reaction. The number of oligonucleotides on a particle, $n(i)$, can be expressed as $n(i) = (4\pi r_p^2/SA)$, where the particle radius, r_p, is $i^{1/3}r_{ion}$, and SA is the surface area of an oligonucleotide. The radius of the PbS ion pair, r_{ion}, is 0.297 nm. From the above equations, the rate of the reaction of A and B is

$$\frac{dA}{dt} = -k_1A^2 + \frac{k_1}{K_1}(AB)_1 - \sum_{i=2}^{N}\left(k_iA^2(AB)_{i-1} - \frac{k_i}{K_i}(AB)_i\right) \quad (4)$$

$$\frac{d(AB)_1}{dt} = k_1A^2 - \frac{k_1}{K_1}(AB)_1 - k_2A^2(AB)_1 + \frac{k_2}{K_2}(AB)_2 - \frac{dC_1}{dt} \quad (5)$$

$$\frac{d(AB)_i}{dt} = k_iA^2(AB)_{i-1} - \frac{k_i}{K_i}(AB)_i - k_{i+1}A^2(AB)_i + \frac{k_{i+1}}{K_{i+1}}(AB)_{i+1} - \frac{dC_i}{dt} \quad (6)$$

The rate of capping and the rate of stable nanoparticle formation can be expressed as follows:

$$\frac{dQ}{dt} = \sum_{i=1}^{N}\left(-n(i)k_q(AB)_iQ^{n(i)} + n(i)\frac{k_q}{K_q}C_i\right) \quad (7)$$

$$\frac{dC_i}{dt} = k_q(AB)_iQ^{n(i)} - \frac{k_q}{K_q}C_i \quad (8)$$

The rates of these reactions can be reduced using the following nondimensional groups: $A = A_0\bar{A}$, $(AB)_i = A_0(\overline{AB})_i$, $C_i = A_0\bar{C}_i$, $Q = A_0\bar{Q}$, $t = (\tau/(k_1A_0))$, $\alpha_i = (k_i/k_1)$, and $\beta = k_q/k_1$. Here, A_0 is the initial concentration of the precursor. Thus, the nondimensionalized equations can be expressed as

$$\frac{d\bar{A}}{d\tau} = -\bar{A}^2 + \frac{1}{A_0K_1}(\overline{AB})_1 - \sum_{i=2}^{N}\left(\alpha_iA_0\bar{A}^2(\overline{AB})_{i-1} - \frac{\alpha_i}{A_0K_i}(\overline{AB})_i\right) \quad (9)$$

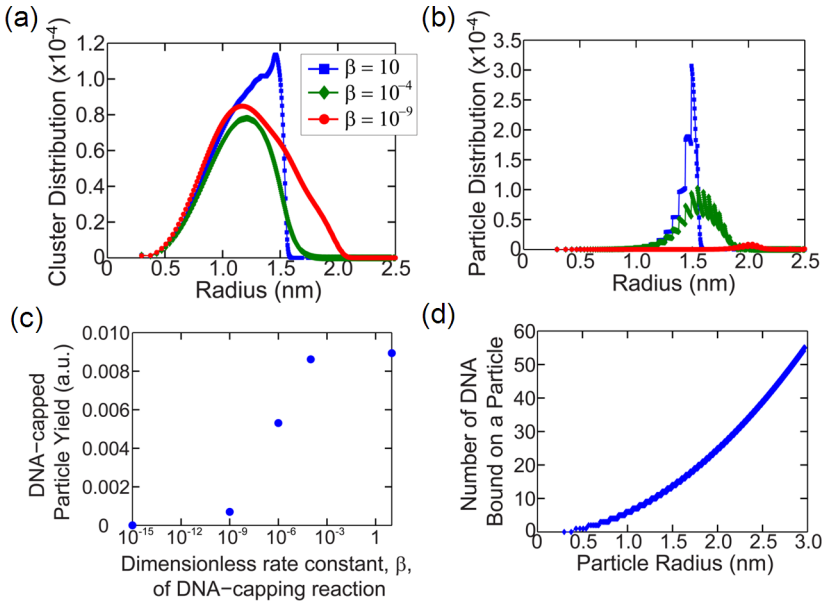

Figure 4. Numerical simulation results of oligonucleotide-templated particle growth examined with DNA surface reactivity as a major parameter. The dimensionless rate constant, β, of the capping reaction indicates the influence of surface reactivity for nucleobase bonding on nanocrystal formation. Size distributions of growing clusters (a) and stable nanocrystals (b). When the reactivity is high (*e.g.*, $\beta = 10$), the population of clusters is converted to stable nanocrystals and the particle size is nearly uniform. In the case of low reactivity ($\beta = 10^{-4}$), the cluster distribution is slightly wider and more symmetric, while the particle distribution becomes notably broader. If the reactivity is negligible ($\beta = 10^{-9}$), the growing clusters have a substantially broader distribution and larger sized particles are formed. (c) Total nanocrystal production as a function of β, showing rapid decrease of the yield below $\beta = 10^{-4}$. The particle yield is determined by integrating the particle distribution function in (b). With no reactivity ($\beta = 0$), no stable nanocrystals are created, consistent with the observation of instantaneous bulk phase precipitation in the absence of DNA ligand. (d) Calculated number of DNA molecules passivating a stable nanocrystal as a function of particle radius.

$$\frac{d(\overline{AB})_i}{d\tau} = \alpha_i A_0 A^2 (\overline{AB})_{i-1} - \frac{\alpha_i}{A_0 K_i}(\overline{AB})_i - \alpha_{i+1} A_0 \bar{A}^2 (\overline{AB})_i + \frac{\alpha_{i+1}}{A_0 K_{i+1}}(\overline{AB})_{i+1} - \frac{d\bar{C}_i}{d\tau} \quad (10)$$

$$\frac{d\bar{Q}}{d\tau} = \sum_{i=1}^{N} \left(-n(i)\beta(\overline{AB})_i \frac{(A_0\bar{Q})^{n(i)}}{A_0} + n(i)\frac{\beta}{A_0 K_q}\bar{C}_i \right) \quad (11)$$

$$\frac{d\bar{C}_i}{d\tau} = \beta(\overline{AB})_i \frac{(A_0\bar{Q})^{n(i)}}{A_0} - \frac{\beta}{A_0 K_q}\bar{C}_i \quad (12)$$

The rate constants are determined from the following expressions:

$$K_i = k_{p,d} \exp\left[-\frac{2\gamma V_m}{rRT}\right] \quad (13)$$

$$\alpha_i = \exp\left[\zeta \frac{2\gamma V_m}{RT}\frac{(r - r_{ion})}{r r_{ion}}\right] \quad (14)$$

Here, R is the universal gas constant and T is the reaction temperature, which is set to 25 °C in the simulations. ζ is the transfer coefficient, which is 0.5, and the surface free energy, γ, is 0.2 J/m^2.[20] V_m is the molar volume of the PbS crystal (3.15×10^{-5} m^3/mol). $k_{p,d}$ and K_q are set to 10^5 and 0.001, respectively. The initial concentrations, A_0 and Q_0, are 2 and 1 mol/m^3, which represents typical experimental conditions. The surface area of DNA, SA, ranges from 10^{-18} (quadruplex) to 10^{-17} m^2 (random chain) and is estimated to be 2×10^{-18} m^2 for calculations. The calculations were performed with the reactivity of nucleobase bonding to the nanocrystal surface as a major parameter. The dimensionless rate constant of the capping reaction, β, is 10 for highly reactive DNA capping and 0 in the absence of DNA template.

By numerically solving the above equations under the conditions undertaken in typical experiments, we obtain distributions of both growing clusters (Figure 4a) and stable nanocrystals (Figure 4b) for several cases. The dimensionless rate constant, β, of the capping reaction indicates the influence of surface reactivity for nucleobase bonding on nanocrystal formation. When the reactivity is high (*e.g.*, $\beta = 10$), the population of clusters is converted to stable particles with no significant population of clusters larger than 3 nm in diameter. The particle distribution is nearly uniform with a diameter of ~3 nm and a fwhm of ~0.24 nm. In the case of low reactivity (*e.g.*, $\beta = 10^{-4}$), the cluster distribution is wider and more symmetric. The particle distribution becomes notably broader with a fwhm of ~0.74 nm in diameter. If the reactivity is negligible (*e.g.*, $\beta = 10^{-9}$), the growing clusters have a substantially broader distribution, and larger sized particles are formed with more than an order of magnitude lower total yield. Here, the particle yield is determined by integrating the particle distribution function

in Figure 4b and plotted in Figure 4c. The particle yield accounts for only the DNA-stabilized nanocrystals, while metastable clusters are not accounted for. The total nanoparticle yield is at its highest for $\beta = 10$, while it decreases rapidly below $\beta = 10^{-4}$. It is necessary to achieve burst nucleation and then particle growth without further nucleation to create nanocrystals with a narrow size distribution. The reactive oligonucleotides provide additional focusing, not allowing clusters to grow larger than ~3 nm in diameter and converting them into stable particles in a narrow size range. These simulation results reasonably describe our experimental observation that oligonucleotide-templated PbS nanocrystals predominantly have a narrow size distribution near 3 nm in diameter, as seen in Figure 1c and d. The simulations also predict that with no reactivity ($\beta = 0$), stable nanocrystals are not created; this is consistent with the observation of instantaneous formation of macroscopic brown precipitates in the absence of oligonucleotide ligands. In contrast, sequences with higher reactivity are able to kinetically trap growing clusters at an intermediate state, resulting in approximately uniform particles, and this is observed experimentally.

The model also captures the effects of changes in the initial conditions. When the reactant molar ratio increases to DNA/S^{2-}/Pb^{2+} = 1:20:40 with all other parameters fixed, the simulation predicts larger particles with a broader size distribution (see Figure S5 in the Supporting Information). These results are similar to what we observed experimentally under the same initial conditions in Figure 1f. Figure 4d shows the number of DNA molecules per particle as a function of particle size, indicating roughly 15 DNA molecules on a 3 nm diameter spherical particle. From optical absorption measurements, we estimate that the number of DNA molecules per particle is in the range of 10 to 30 after the washing process to remove excess DNA ligands (also see the Supporting Information). Our kinetic model provides overall predictions between particle structure and DNA–surface reactivity during the DNA-mediated particle growth processes. Further studies could elucidate the correlation between DNA sequences and their reactivity.

CONCLUSION

We have elucidated the growth mechanisms of oligonucleotide-templated nanocrystals and investigated their surface properties. Our results suggest that amine and carbonyl groups are responsible for surface passivation, and steric and/or secondary conformation effects of the capping strands play an important role in stabilizing the colloids. This study also indicates that overall surface reactivity of the sequences predominantly determines the quality of the resulting particles. Our mechanistic study presents the foundation of oligonucleotide-templated synthesis, which could lead to nanoparticles with built-in molecular recognition capabilities. The oligonucleotide-based approach is as facile and versatile as other biomolecular nanofabrication methodologies, like those for peptides or viruses.[37,38] We envision that this approach may be further developed by designing nucleic acids that have two distinct domains of nanoparticle binding/growth and target recognition. With much to be explored at the bioorganic–inorganic interface, these materials should be useful in biological sensing and imaging as well as many other applications.

METHODS

Oligonucleotide-Templated Nanocrystal Synthesis. All oligonucleotide sequences used were custom-synthesized and obtained from IDT, Inc. Particle synthesis was carried out in open air at room temperature. For typical lead sulfide nanocrystal synthesis, 20 nmol of DNA and 80 nmol of lead(II) acetate (Aldrich) were mixed in filtered deionized water (pH 6.5) or 1× TAE buffer without EDTA (pH 8.0). The colorless solution became light brown upon addition of 40 nmol of sodium sulfide (Aldrich) with vigorous stirring. The concentrations of the precursor molecules varied, but the final molar ratio of DNA/S^{2-}/Pb^{2+} was fixed at 1:2:4 unless denoted otherwise. We examined 10 different single-stranded DNA sequences for nanocrystal synthesis: poly GT: $d(GT)_{15}$, $d(GT)_{10}$, or $d(GT)_5$; thrombin-binding aptamer or TBA: $^{5'}$GGT TGG TGT GGT TGG$^{3'}$; AS1411: $^{5'}$GGT GGT GGT GGT TGT GGT GGT GGT GG$^{3'}$; poly C: dC_{30}; poly T: dT_{30}; poly G_4T: $d(GGGGT)_6$; poly GC: $d(GC)_{15}$; poly A: dA_{30}.

For Fe_3O_4 nanocrystal synthesis, 20 nmol of DNA was mixed in a solution of ferric and ferrous chloride (Fisher) at a ratio of DNA/Fe^{2+}/Fe^{3+} = 1:4:8 unless indicated otherwise. Approximately 10 μL of ammonia hydroxide (Fisher) was added to achieve ~pH 10, initiating formation of Fe_3O_4 nanocrystals. As-synthesized chalcogenide and iron oxide nanocrystals were washed to remove unbound excess DNA and ions by adding an equi-volume mixture solution of 3 M NaCl and 2-propanol (4 times greater than the particle solution in volume), followed by vigorous vortexing and centrifugation at 16.3*g* for 4 min. The colorless supernatant was discarded, and the brown pellet was redispersed by 30 s bath sonication.

Characterization of Synthesized Nanocrystals. A Horiba JY Fluorolog-3 spectrofluorometer with a liquid N_2-cooled InGaAs detector measured near-IR emission from PbS nanocrystals. For FTIR measurement, free DNA and washed DNA-templated nanocrystals prepared in D_2O were deposited on polyethylene IR cards (Thermo Electron) and dried in a vacuum chamber. The spectra were obtained using a Thermo Nicolet Magna-IR 760 spectrometer at a resolution of 0.5 cm^{-1} with a blank IR card as background.

TBA-capped PbS and Fe_3O_4 nanocrystals were visualized by a JEOL 2010 LaB6 TEM with an acceleration voltage of 200 kV, while the PbS nanocrystals synthesized with 30-mer poly GT DNA were imaged by 80–300 kV S/TEM FEI Titan operated at 300 kV. A drop of diluted particle solution was deposited on a TEM copper grid with a carbon thin film (Tedpella) and dried before characterization. Dynamic light scattering (Brookhaven Instruments Corp., 200SM) was employed to measure hydrodynamic diameters of DNA-capped particles using an excitation of 514 nm (Lexel Ar^+ laser).

Conflict of Interest: The authors declare no competing financial interest.

Acknowledgment. The authors thank Dmitry Zemlyanov of the Surface Analysis Facility at Birck Nanotechnology Center for

XPS measurements. This work was supported by National Science Foundation (NSF) and Office of Naval Research (ONR). J.H.C. acknowledges an NSF CAREER Award. M.S.S. expresses his gratitude to the NSF and Beckman Young Investigator Awards. J.-H.H. appreciates support from Agency for Defense Development through the Chemical & Biological Defence Research Center and Gachon University. K.H.C. acknowledges the National Science Scholarship from the Agency for Science, Technology and Research of Singapore.

Supporting Information Available: Additional experimental details. This material is available free of charge *via* the Internet at http://pubs.acs.org.

REFERENCES AND NOTES

1. Katz, E.; Willner, I. Integrated Nanoparticle–Biomolecule Hybrid Systems: Synthesis, Properties, and Applications. *Angew. Chem., Int. Ed.* **2004**, *43*, 6042–6108.
2. Alivisatos, A. P. The Use of Nanocrystals in Biological Detection. *Nat. Biotechnol.* **2004**, *22*, 47–52.
3. Medintz, I. L.; Uyeda, H. T.; Goldman, E. R.; Mattoussi, H. Quantum Dot Bioconjugates for Imaging, Labelling and Sensing. *Nat. Mater.* **2005**, *4*, 435–446.
4. Kim, S.; Lim, Y. T.; Soltesz, E. G.; De Grand, A. M.; Lee, J.; Nakayama, A.; Parker, J. A.; Mihaljevic, T.; Laurence, R. G.; Dor, D. M.; *et al*. Near-Infrared Fluorescent Type II Quantum Dots for Sentinel Lymph Node Mapping. *Nat. Biotechnol.* **2004**, *22*, 93–97.
5. Gao, X.; Cui, Y.; Levenson, R. M.; Chung, L. W. K.; Nie, S. *In Vivo* Cancer Targeting and Imaging with Semiconductor Quantum Dots. *Nat. Biotechnol.* **2004**, *22*, 969–976.
6. Weissleder, R.; Moore, A.; Mahmood, U.; Bhorade, R.; Benveniste, H.; Chiocca, E. A.; Basilion, J. P. *In Vivo* MR Imaging of Transgene Expression. *Nat. Med.* **2000**, *6*, 351–354.
7. Zhang, T.; Ge, J.; Hu, Y.; Yin, Y. A General Approach for Transferring Hydrophobic Nanocrystals into Water. *Nano Lett.* **2007**, *7*, 3203–3207.
8. Gao, X.; Yang, L.; Petros, J. A.; Marshall, F. F.; Simons, J. W.; Nie, S. *In Vivo* Molecular and Cellular Imaging with Quantum Dots. *Current Opinion in Biotechnology* **2005**, *16*, 63–72.
9. Baker, B. A.; Choi, J. H. Oligonucleotide DNA and RNA as Direct Capping Ligand for Nanocrystals: An Emerging Method for Biological Diagnostics and Therapeutics. *Nano* **2009**, *4*, 189–199.
10. Berti, L.; Burley, G. A. Nucleic Acid and Nucleotide-Mediated Synthesis of Inorganic Nanoparticles. *Nat. Nanotechnol.* **2008**, *3*, 81–87.
11. Feldheim, D. L.; Eaton, B. E. Selection of Biomolecules Capable of Mediating the Formation of Nanocrystals. *ACS Nano* **2007**, *1*, 154–159.
12. Choi, J. H.; Chen, K. H.; Strano, M. S. Aptamer-Capped Nanocrystal Quantum Dots: A New Method for Label-Free Protein Detection. *J. Am. Chem. Soc.* **2006**, *128*, 15584–15585.
13. Choi, J. H.; Chen, K. H.; Han, J. H.; Chaffee, A. M.; Strano, M. S. DNA Aptamer-Passivated Nanocrystal Synthesis: A Facile Approach for Nanoparticle-Based Cancer Cell Growth Inhibition. *Small* **2009**, *5*, 672–675.
14. Ma, N.; Yang, J.; Stewart, K. M.; Kelley, S. O. DNA-Passivated CdS Nanocrystals: Luminescence, Bioimaging, and Toxicity Profiles. *Langmuir* **2007**, *23*, 12783–12787.
15. Green, M.; Taylor, R.; Wakefield, G. The Synthesis of Luminescent Adenosine Triphosphate Passivated Cadmium Sulfide Nanoparticles. *J. Mater. Chem.* **2003**, *12*, 1859–1861.
16. Ma, N.; Sargent, E. H.; Kelley, S. O. One-Step DNA-Programmed Growth of Luminescent and Biofunctionalized Nanocrystals. *Nat. Nanotechnol.* **2008**, *4*, 121–125.
17. Hinds, S.; Taft, B. J.; Levina, L.; Sukhovatkin, V.; Dooley, C.; Roy, M. D.; MacNeil, D. D.; Sargent, E. H.; Kelley, S. O. Nucleotide-Directed Growth of Semiconductor Nanocrystals. *J. Am. Chem. Soc.* **2006**, *128*, 64–65.
18. Gugliotti, L. A.; Feldheim, D. L.; Eaton, B. E. RNA-Mediated Metal-Metal Bond Formation in the Synthesis of Hexagonal Palladium Nanoparticles. *Science* **2004**, *304*, 850–852.
19. Ma, N.; Dooley, C. J.; Kelley, S. O. RNA-Templated Semiconductor Nanocrystals. *J. Am. Chem. Soc.* **2006**, *128*, 12598–12599.
20. Park, J.; Joo, J.; Kwon, S. G.; Jang, Y.; Hyeon, T. Synthesis of Monodisperse Spherical Nanocrystals. *Angew. Chem., Int. Ed.* **2007**, *46*, 4630–4660.
21. Bock, L. C.; Griffin, L. C.; Latham, J. A.; Vermaas, E. H.; Toole, J. J. Selection of Single-Stranded DNA Molecules That Bind and Inhibit Human Thrombin. *Nature* **1992**, *355*, 564–566.
22. Bates, P. J.; Kahlon, J. B.; Thomas, S. D.; Trent, J. O.; Miller, D. M. Antiproliferative Activity of G-rich Oligonucleotides Correlates with Protein Binding. *J. Biol. Chem.* **1999**, *274*, 26369–26377.
23. Teng, Y.; Girvan, A. C.; Casson, L. K.; Pierce, J. W. M.; Qian, M.; Thomas, S. D.; Bates, P. J. AS1411 Alters the Localization of a Complex Containing Protein Arginine Methyltransferase 5 and Nucleolin. *Cancer Res.* **2007**, *67*, 10491–10500.
24. Kane, R. S.; Cohen, R. E.; Silbey, R. Theoretical Study of the Electronic Structure of PbS Nanocluster. *J. Phys. Chem.* **1996**, *100*, 7928–7932.
25. Coffer, J. L.; Bigham, S. R.; Pinizzotto, R. F.; Yang, H. Characterization of Quantum Confined CdS Nanocrystallites Stabilized by Deoxyribonucleic Acid (DNA). *Nanotechnology* **1992**, *3*, 69–76.
26. Green, M.; Smyth-Boyle, D.; Harries, J.; Taylor, R. Nucleotide Passivated Cadmium Sulfide Quantum Dots. *Chem. Commun.* **2005**, 4830–4832.
27. Dong, L.; Hollis, T.; Connolly, B. A.; Wright, N. G.; Horrocks, B. R.; Houlton, A.; Templated, D. N. A. Semiconductor Nanoparticle Chains and Wires. *Adv. Mater.* **2007**, *19*, 1748–1751.
28. Mornet, S.; Vekris, A.; Bonnet, J.; E., D.; Grasset, F.; Choy, J.-H.; Portier, J. DNA-Magnetite Nanocomposite Materials. *Mater. Lett.* **2000**, *42*, 183–188.
29. Nyamjav, D.; Ivanisevic, A. Templates for DNA-Templated Fe_3O_4 Nanoparticles. *Biomaterials* **2005**, *26*, 2749–2757.
30. Jana, N. R.; Chen, Y.; Peng, X. Size- and Shape-Controlled Magnetic (Cr, Mn, Fe, Co, Ni) Oxide Nanocrystals *via* a Simple and General Approach. *Chem. Mater.* **2004**, *16*, 3931–3935.
31. Roca, A. G.; Morales, M. P.; Serna, C. J. Synthesis of Monodispersed Magnetite Particles from Different Organometallic Precursors. *IEEE Trans. Magn.* **2006**, *42*, 3025–3029.
32. Santamaria, R.; Charro, E.; Zacarias, A.; Castro, M. Vibrational Spectra of Nucleic Acid Bases and Their Watson-Crick Pair Complexes. *J. Comput. Chem.* **1999**, *20*, 511–530.
33. Mondragon-Sanchez, J. A.; Liquier, J.; Shafer, R. H.; Taillandier, E. Tetraplex Structure Formation in the Thrombin-Binding DNA Aptamer by Metal Cations Measured by Vibrational Spectroscopy. *J. Biomol. Struct. Dyn.* **2004**, *22*, 365–373.
34. Guzman, M. R.; Liquier, J.; Brahmachari, S. K.; Taillandier, E. Characterization of Parallel and Antiparallel G-tetraplex Structures by Vibrational Spectroscopy. *Spectrochim. Acta, Part A* **2006**, *64*, 495–503.
35. Banyay, M.; Sarkar, M.; Graslund, A. A Library of IR Bands of Nucleic Acids in Solution. *Biophys. Chem.* **2003**, *104*, 477–488.
36. Mandal, H. S.; Kraatz, H.-B. Effect of the Surface Curvature on the Secondary Structure of Peptides Adsorbed on Nanoparticles. *J. Am. Chem. Soc.* **2007**, *129*, 6356–6357.
37. Sarikaya, M.; Tamerler, C.; Jen, A. K.-Y.; Schulten, K.; Baneyx, F. Molecular Biomimetics: Nanotechnology through Biology. *Nat. Mater.* **2003**, *2*, 577–585.
38. Mao, C.; Solis, D. J.; Reiss, B. D.; Kottmann, S. T.; Sweeney, R. Y.; Hayhurst, A.; Georgiou, G.; Iverson, B.; Belcher, A. M. Virus-Based Toolkit for the Directed Synthesis of Magnetic and Semiconducting Nanowires. *Science* **2004**, *303*, 213–217.